

# Uniform Reanalysis of JWST MIRI 15 $\mu$ m Exoplanet Eclipse Observations using Frame-Normalized Principal Component Analysis

NICHOLAS J. CONNORS,<sup>1</sup> CHRISTOPHER MONAGHAN,<sup>1</sup> BJÖRN BENNEKE,<sup>2,1</sup> AND LISA DANG<sup>1</sup>

<sup>1</sup>*Department of Physics and Trottier Institute for Research on Exoplanets, Université de Montréal, Montreal, QC, Canada*

<sup>2</sup>*Department of Earth, Planetary, and Space Sciences, University of California, Los Angeles, CA, USA*

## ABSTRACT

JWST MIRI 15 $\mu$ m time-series eclipse photometry presents a powerful way to probe for the presence of atmospheres on low-temperature rocky exoplanets orbiting nearby stars. Here, we introduce a novel technique, frame-normalized principal component analysis (FN-PCA) to analyze and detrend these MIRI time-series observations. Using the FN-PCA technique, we perform a uniform reanalysis of the published MIRI 15 $\mu$ m observations of LHS 1478 b, TOI-1468 b, LHS 1140 c, TRAPPIST-1 b, and TRAPPIST-1 c using our new data reduction pipeline (*Erebus*) and compare them to different potential atmospheric and surface compositions. We also investigate additional public data sets with the sole purpose of understanding the instrument systematics affecting MIRI. We identify and categorize important detector-level systematics in the observations that are generally present across all 17 analyzed eclipse observations, which we illustrate as eigenimage/eigenvalue pairs in the FN-PCA. One of these eigenimage/eigenvalue pairs corresponds to the prominent ramp effect at the beginning of the time-series observations which has widely been reported for JWST and Spitzer photometry. For JWST/MIRI, we show that the detector settling time scales exponentially with the apparent magnitude of the target star  $T_{\text{set}} [\text{hours}] = 0.063 \exp^{0.427 \cdot m_K} - 0.657$ . This uniform reanalysis and investigation of JWST/MIRI systematics is done in preparation for the 500 hour Rocky Worlds DDT survey, to demonstrate a data-driven systematic model usable across all MIRI 15 $\mu$ m datasets.

**Keywords:** Exoplanets (498); Exoplanet atmospheres (487); Planetary atmospheres (1244)

## 1. INTRODUCTION

Among the known rocky exoplanets, those around M-dwarfs are considered the best small targets for atmospheric characterization. The low temperatures of these stars allow habitable zone exoplanets to orbit with short periods, giving frequent opportunities to observe temperate planets in eclipse (Redfield et al. 2024, Nutzman & Charbonneau 2008). Additionally, low-mass dwarf-type stars are the most common star type in our galaxy, giving an abundance of targets for characterization (Bochanski et al. 2010). However, the stellar activity of these stars may make it difficult for planets orbiting them to form or sustain atmospheres (Luger & Barnes 2015). Understanding if this population of planets can have atmospheres is therefore an important step in the search for habitable worlds similar to our own (Redfield et al. 2024, de Wit et al. 2024).

Secondary eclipse photometry using the MIRI instrument at 15 $\mu$ m on board the James Webb Space Tele-

scope allows us to infer the atmospheric and surface composition of rocky exoplanets without being subject to stellar contamination found in exoplanet transit observations (Rackham et al. 2018, Zieba et al. 2023, Greene et al. 2023, August et al. 2024, Valdés et al. 2025, Fortune et al. 2025). Despite the effects of tidal locking, atmospheric models predict that it is still possible for these short-period planets orbiting M dwarfs to maintain atmospheres (Turbet, Martin et al. 2018). The presence of an atmosphere allows for heat-redistribution from the day-side to the night-side, resulting in a shallower eclipse depth compared to the bare rock scenario (Koll 2022, Coy et al. 2025).

Measurements of secondary eclipses require high precision to distinguish between the different atmospheric or surface composition models for a given planet. For secondary eclipse observations performed using MIRI F1500W it is important to understand the systematic noise of the instrument to improve precision (Zieba et al. 2023, Greene et al. 2023, August et al. 2024, Valdés et al. 2025, Fortune et al. 2025).

So far there have been two completed JWST programs performing MIRI 15 $\mu$ m secondary eclipse photometry

to infer the atmospheric compositions of rocky exoplanets orbiting M-dwarf stars: TRAPPIST-1 b (GTO-1177 [Greene et al. 2023](#)) and TRAPPIST-1 c (GO-2304 [Zieba et al. 2023](#)). There has also been a full phase curve observation of TRAPPIST-1b and c using the same instrument (GO-3077). There are currently two more secondary-eclipse programs in-progress: The Hot Rocks Survey observing 9 exoplanets (GO-3730 [August et al. 2024](#), [Valdés et al. 2025](#)) and a program for observing the potentially volcanically active rocky exoplanet LP 791-18 d (GO-6457 [Benneke et al. 2024](#)). Future observations include a recently approved Cycle 4 program to follow up on previous observations of LHS 1478 b using MIRI LRS and F1500W (GO-7675 [August et al. 2025](#)), and the 500 hour Rocky Worlds Director’s Discretionary Time survey which will investigate a number of rocky exoplanets in combination with the Hubble Space Telescope ([Redfield et al. 2024](#)). The targets LTT 1445 A c, LTT 1445 A b, LHS 1140 b, and GJ 3929 b are already announced for this survey.

The currently published MIRI 15 $\mu$ m secondary eclipse literature uses a variety of methods to detrend against systematic noise. This includes using polynomials from the 0th to 3rd degree of time, polynomials of the Gaussian centroid positions and widths, exponential ramps in time, Gaussian processes, and linear combinations of up to 36 pixel time-series, as well as different combinations of each ([Zieba et al. 2023](#), [Greene et al. 2023](#), [August et al. 2024](#), [Valdés et al. 2025](#)). The final choice of which combination of models to use is then justified by goodness of fit metrics, and all models are parametric and make assumptions on the behaviour of the instrument noise.

In this paper we present **Erebus**, a new data analysis pipeline for JWST/MIRI photometric data of transiting exoplanets, and use it to analyze F1500W data. It uses a novel data-driven method of detrending lightcurves against systematic noise: Frame-Normalized Principal Component Analysis (FN-PCA). We perform principal component analysis on the time-series image observations of a star during a secondary eclipse, after normalizing by the total intensity of each frame. This removes the effects of astrophysical signals (e.g., the eclipse itself and stellar variability) from the eigenvalues generated by the PCA, as we expect such signals to show as uniform increases/decreases in intensity across the entire detector. We detrend the lightcurve against the time-series eigenvalues of the top 5 principal components found for each dataset, which represent pixel-level systematics of the detector during the observation. While we only use it for F1500W data in this paper, **Erebus** is generally applicable to the other MIRI filters, notably the F1280W

filter which has also been used for secondary eclipse observations ([Ducrot et al. 2024](#)).

PCA is a data-analysis tool which reduces the dimensionality of a data set by re-expressing it as a linear combination of eigenvalue/eigenvector pairs called principal components. These principal components are ranked in order of variance, so that those with a lower variance are classified as noise and those with a higher variance are classified as important signals. The principal components are selected such that they are all orthogonal to each other. This technique is used to find underlying structures in otherwise confusing datasets ([Shlens 2014](#)).

Past analyses of JWST exoplanet time series observations have shown that small changes in PSF morphology can be precisely tracked via principal component analysis of the detector images, proving useful in detrending against distinct sources of instrumental noise ([Ahler et al. 2025](#), [Coulombe et al. 2023, 2025](#), [Radica et al. 2024, 2025](#)).

We use this new method to reanalyze existing secondary eclipse observations performed with MIRI Imaging F1500W for the planets LHS 1478 b ([August et al. 2024](#)), TOI-1468 b ([Valdés et al. 2025](#)), LHS 1140 c ([Fortune et al. 2025](#)), TRAPPIST-1 b ([Greene et al. 2023](#)), and TRAPPIST-1 c ([Zieba et al. 2023](#)).

This paper is divided into 5 sections. Section 2 will describe the methodology used for extracting secondary eclipse lightcurves which are then detrended and analyzed using FN-PCA. Section 3 will show how the principal components found using FN-PCA give us insights into telescope and detector systematics. Section 4 will compare our results to different potential atmospheric and surface compositions of the five planets we reanalyzed. Section 5 summarizes our conclusions.

## 2. DATA ANALYSIS

When extracting the photometric data we use the `jwst` pipeline ([Bushouse et al. 2022](#)) stage 2 outputs (`_calints.fits`) available on the Mikulski Archive for Space Telescopes (MAST). For a single visit of TRAPPIST-1b (visit 5) we find the default stage 2 `jwst` output on MAST to be unusable, and instead use the default stage 2 output of the **Eureka!** pipeline ([Bell et al. 2022](#)) ran on the uncalibrated fits data from MAST. We measure the flux within a five pixel radius aperture, and use an annulus spanning 12 to 20 pixels to perform background subtraction without overlapping the airy ring. We choose to use a uniform five pixel aperture across all data sets based on the optimal aperture sizes found in previous literature ([Greene et al. 2023](#), [August et al. 2024](#), [Valdés et al. 2025](#), [Fortune et al. 2025](#)) and additionally try a four pixel aperture

**Table 1.** Orbital parameters used to determine Gaussian priors.

Planet	$t_0$ (BJD-2,450,000)	$P$ (days)	$R_p/R_*$	$a/R_*$	$i$ (deg)	$e$	$\omega$ (deg)
TRAPPIST-1 b	*	1.51088432(15) <sup>(1)</sup>	0.08590(37) <sup>(2)</sup>	20.843 <sup>+0.094</sup> <sub>-0.155</sub> <sup>(2)</sup>	89.728(165) <sup>(2)</sup>	0.00622(304) <sup>(7)</sup>	336.86 ± 34.24 <sup>(7)</sup>
TRAPPIST-1 c	*	2.42179346(23) <sup>(1)</sup>	0.08440(38) <sup>(2)</sup>	28.549 <sup>+0.129</sup> <sub>-0.212</sub> <sup>(2)</sup>	89.778(118) <sup>(2)</sup>	0.00654(188) <sup>(7)</sup>	282.45 ± 17.10 <sup>(7)</sup>
TOI-1468 b	8765.68079 <sup>+0.00070</sup> <sub>-0.00069</sub> <sup>(3)</sup>	1.8805136 <sup>+0.0000024</sup> <sub>-0.0000026</sub> <sup>(3)</sup>	0.03411(15) <sup>(3)</sup>	13.14 <sup>+0.21</sup> <sub>-0.24</sub> <sup>(3)</sup>	88.47 <sup>+0.34</sup> <sub>-0.29</sub> <sup>(3)</sup>	-	-
LHS 1478 b	8786.75425(42) <sup>(4)</sup>	1.9495378 <sup>+0.0000040</sup> <sub>-0.0000041</sub> <sup>(4)</sup>	0.0462 <sup>+0.0011</sup> <sub>-0.0010</sub> <sup>(4)</sup>	16.119 <sup>+0.088</sup> <sub>-0.094</sub> <sup>(4)</sup>	87.452 <sup>+0.052</sup> <sub>-0.048</sub> <sup>(4)</sup>	-	-
LHS 1140 c	8389.2939(2) <sup>(5)</sup>	3.777940(2) <sup>(5)</sup>	0.05486(13) <sup>(6)</sup>	26.57(5) <sup>(6)</sup>	89.80(19) <sup>(5)</sup>	-	-

NOTE—The larger value was used as standard deviation for the prior when the reported uncertainties are asymmetric.

\*: To account for transit-timing variation, we use the closest forecasted transit time calculated in Agol et al. (2024) for each individual visit of TRAPPIST-1 b and c.

**References:** (1) Ducrot et al. (2020), (2) Agol et al. (2021), (3) Chaturvedi et al. (2022), (4) Soto et al. (2021), (5) Cadieux et al. (2023), (6) Kokori et al. (2023), (7) Grimm et al. (2018)

closer to the size used in Zieba et al. (2023) but find the difference in eclipse depths between the two sizes to be negligible. We mask out values marked DO NOT USE and  $3\sigma$  outliers and replace them with 2d linearly interpolated data within the affected frame. From this we get the raw lightcurve (shown in the top panel of Figure 1) using aperture photometry which we later detrend with our FN-PCA approach.

We perform the FN-PCA of the background-subtracted time-series image data using PCA from the `sklearn` Python library (Pedregosa et al. 2011) with each frame normalized in order to avoid fitting out the eclipse itself. For each principal component we get a time-series of eigenvalues and an eigenimage (Figure 1, right). The first five principal components (ranked in order of significance i.e., how much of the variance they explain) are used to detrend the lightcurve. We fit five coefficients (one per principal component) with uninformative uniform priors (from  $-10$  to  $10$ ) to create our systematic model which linearly detrends the data against the eigenvalues expressed in parts-per-million. This systematic model is multiplied by a linear slope to account for changes in stellar brightness over the observation. The principal component detrending is intended to model the systematic noise inherent in the instrument, while the linear component is to account for long-term astrophysical trends.

The systematic model is:

$$F_{sys} = (1 + \sum_{i=1}^5 c_i \lambda_i)(at + b) \quad (1)$$

where  $c_i$  is the coefficient for the  $i$ th eigenvalue  $\lambda_i$ , and  $a$  and  $b$  are the coefficients for a 1st degree polynomial.

When fitting for the light curve we use a `batman` model (Kreidberg 2015) multiplied by our systematic model. We use Gaussian priors on the mid-transit time  $t_0$ , or-

bital period length  $P$ , planet radius  $R_p$ , semi-major axis  $a$ , inclination  $i$ , as well as the eccentricity and longitude of periastron with  $e \cos \omega$  and  $e \sin \omega$  based on the error-bars of the latest values found on the exoplanet archive (see Table 1). We use an uninformative uniform prior for the eclipse depth from  $-2000$  to  $2000$  ppm. This prior allows for negative eclipse depth values to not artificially bias the fitting towards eclipse detections. We use  $e \cos \omega$  to fit for the eclipse time offset from a perfectly circular orbit as described in Charbonneau et al. (2005):

$$\Delta t_{eclipse} \approx \frac{2P}{\pi} e \cos \omega. \quad (2)$$

We perform our fitting using a Markov chain Monte Carlo (MCMC) using the `emcee` Python library (Foreman-Mackey et al. 2013). For each visit, we check for convergence by running two chains in parallel and testing the Gelman-Rubin statistic (Gelman & Rubin 1992) to see that they have converged to the same value, and we test that the length of the chains is at least 50 times greater than the autocorrelation times of all parameters.

We perform individual fits for each visit and a joint fit for each planet. For the joint fits we bin the data from each visit by four, and we fix most orbital parameters to their values in Table 1 fitting only for shared values of  $e \cos \omega$  and  $e \sin \omega$  to fit for the eclipse timing offset (unless assuming a circular orbit),  $f_p$  for the shared eclipse depth, and individual systematic parameters for each visit.

We ran our eclipse depth pipeline on LHS 1478 b, TOI-1468 b, LHS 1140 c, TRAPPIST-1 b, and TRAPPIST-1 c data. For TRAPPIST-1 b and c we fit for the eccentricity of their orbits. For the other planets we model them as entirely circular as the uncertainty in their mid-transit times and periods allow for a wider range of possible eclipse times. We discard the first and last 10 in-

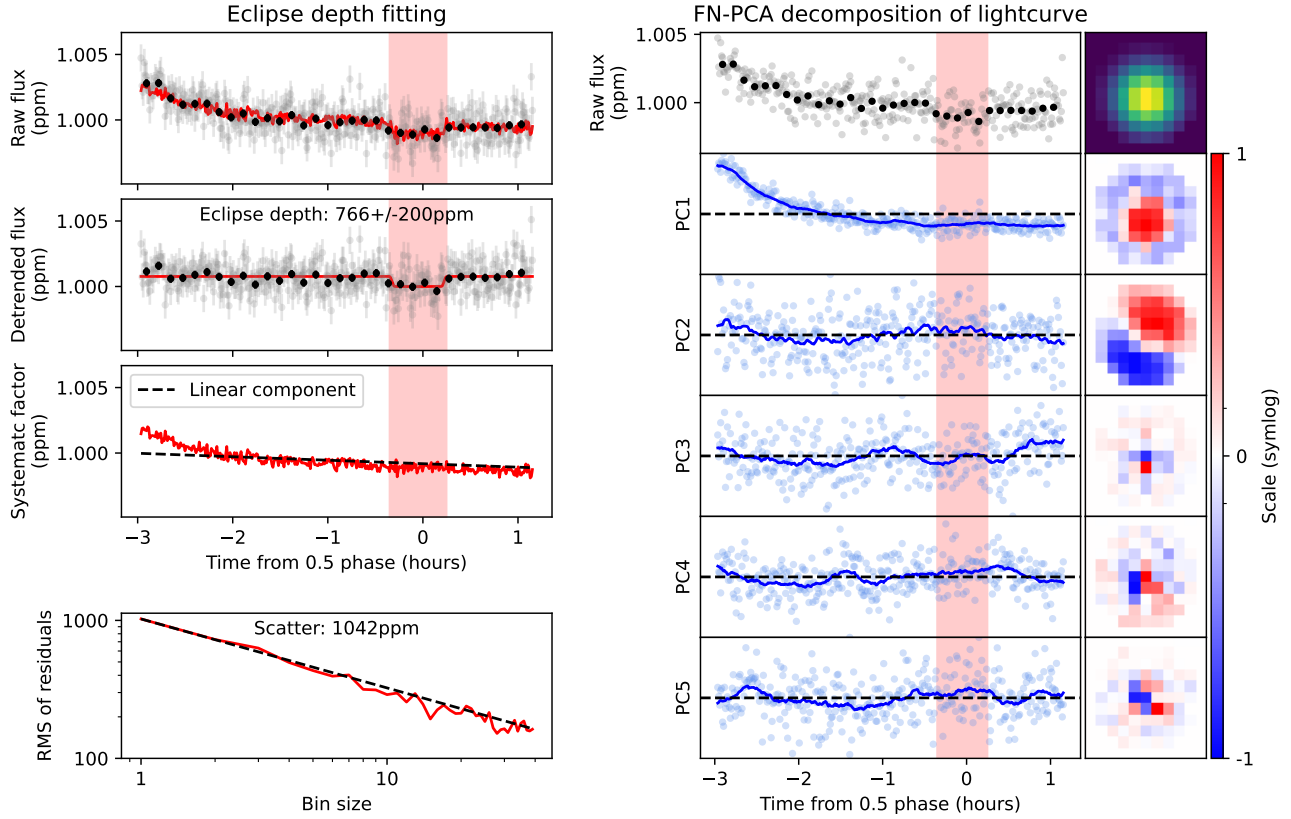


**Figure 1.** Frame normalized principal component analysis (FN-PCA) detrending fit for TRAPPIST-1b visit 1 using the *Erebus* pipeline. The panels on the left, from top to bottom, show the raw lightcurve produced by our pipeline, the detrended light-curve using the FN-PCA systematic model, a breakdown of the linear and PCA components of the systematic model, and a plot comparing the root mean squared of residuals depending on bin size showing the goodness of fit compared to the ideal case (dotted-line). The panels on the right show the raw lightcurve and point spread function (first row), and the eigenvalue and eigenimages for the top 5 principal components explaining most of the variance (rows 2 to 6). The dashed line on the eigenvalue plots shows where the value is 0. As the dimmest star analyzed, we see the detector-settling component (3.1) is the most prominent principal component (PC1), followed by the positive-diagonal centroiding component (PC2) (3.2). The negative-diagonal centroiding component is not present, and the remaining principal components are pixel-dominated (PC3) (3.3) or random (PC 4 and 5) (3.4). The predicted eclipse is shown as the red area centered around 0.5 phase.

tegrations of each visit. For LHS 1478 b we discard the last 40, as both of its visits have large systematic effects at the end of the observation as seen in [August et al. \(2024\)](#). We detrend the data against the first five principal components found by FN-PCA (Figure 1), and then against an exponential ramp for comparison. We compare these results to the results in the literature in Figure 2, with exact values in Table 2.

### 2.1. LHS 1478 b

For LHS 1478 b visit 2 we are unable to detect an eclipse, much like in the original Hot Rocks survey paper ([August et al. 2024](#)). This supports the conclusion from [August et al. \(2024\)](#) that the “sinusoidal systematic” they observe during the predicted eclipse time is likely astrophysical in origin, as our FN-PCA detrend-

ing is (by design) unable to detect astrophysical signals and does not show signs of sinusoidal variation.

### 2.2. TOI-1468 b

The results from *Erebus* show that the first visit of TOI-1468 b is shallower than the other two by  $2\sigma$  (Figure 2). The results shown in [Valdés et al. \(2025\)](#) also have this eclipse being shallower than the others. Our result for the two deep visits and the joint fit agrees with [Valdés et al. \(2025\)](#) within  $1\sigma$ , although for the first visit we find an eclipse depth that is lower by  $\geq 1\sigma$ . In [Valdés et al. \(2025\)](#) they list a number of potential causes for why the first visit in particular was significantly shallower.

### 2.3. LHS 1140 c

For LHS 1140 c we get eclipse depths that are within  $1\sigma$  of those found in [Fortune et al. \(2025\)](#). The mean

**Table 2.** Eclipse depths from this work compared to literature values.

Planet	Visit #	FN-PCA (ppm)	Exponential (ppm)	Literature (ppm)
<b>LHS 1478 b</b>	1	$173 \pm 69$	$166 \pm 70$	$146 \pm 56$
	2	$-145 \pm 71$	$-160 \pm 68$	-
	Mean	$14 \pm 50$	$3 \pm 49$	$146 \pm 56$
	Joint Fit	$-11 \pm 51$	$-0 \pm 50$	$86 \pm 66$
<b>TOI-1468 b</b>	1	$168 \pm 64$	$157 \pm 52$	$239^{+50}_{-53}$
	2	$354 \pm 58$	$338 \pm 51$	$341^{+52}_{-53}$
	3	$369 \pm 55$	$366 \pm 50$	$357^{+52}_{-52}$
	Mean	$297 \pm 34$	$287 \pm 30$	$312^{+30}_{-30}$
	Joint Fit	$286 \pm 39$	$281 \pm 30$	$311^{+31}_{-30}$
<b>LHS 1140 c</b>	1	$281 \pm 59$	$305 \pm 60$	$327 \pm 82$
	2	$197 \pm 57$	$203 \pm 53$	$215 \pm 75$
	3	$233 \pm 60$	$298 \pm 53$	$272 \pm 79$
	Mean	$237 \pm 34$	$269 \pm 32$	$271 \pm 45$
	Joint Fit	$242 \pm 35$	$263 \pm 32$	$273 \pm 43$
<b>TRAPPIST-1 b</b>	1	$780 \pm 191$	$733 \pm 192$	$790 \pm 220$
	2	$1044 \pm 192$	$1132 \pm 178$	$510 \pm 210$
	3	$599 \pm 217$	$474 \pm 219$	$950 \pm 220$
	4	$728 \pm 216$	$608 \pm 225$	$820 \pm 220$
	5	$795 \pm 170$	$727 \pm 180$	$820 \pm 200$
	Mean	$789 \pm 88$	$735 \pm 89$	$778 \pm 96$
	Joint Fit	$863 \pm 90$	$823 \pm 83$	$861 \pm 99$
<b>TRAPPIST-1 c</b>	1	$-131 \pm 211$	$-109 \pm 190$	$445 \pm 193$
	2	$301 \pm 202$	$435 \pm 230$	$418 \pm 173$
	3	$335 \pm 199$	$302 \pm 193$	$474 \pm 158$
	4	$1064 \pm 177$	$753 \pm 187$	$459 \pm 185$
	Mean	$393 \pm 98$	$345 \pm 100$	$449 \pm 89$
	Joint Fit	$312 \pm 128$	$306 \pm 113$	$431^{+97}_{-96}$

NOTE—When a paper presents multiple results from different data reduction methods we specify the exact result we are referring to in the literature. TRAPPIST-1 b literature results are from [Greene et al. \(2023\)](#), the joint-fit result is their adopted value and the individual fits are from “individual fits no. 1”. TRAPPIST-1 c literature results are from [Zieba et al. \(2023\)](#), the individual fit results are from data analysis “ED”, and the joint fit result is from data analysis “SZ”. TOI-1468 b literature results are from [Valdés et al. \(2025\)](#). LHS 1478 b literature results are from [August et al. \(2024\)](#), the joint-fit result is from section 4.3 “Joint fit with *juliet*”, and no result is given for visit 2 (only an upper bound of 300ppm) due to systematic noise. LHS 1140 c literature results are from the “GP aperture extraction” fits in [Fortune et al. \(2025\)](#). Eclipse depth results are visualized in Figure 2.

and joint fit results of our exponential fit are closer to the “GP aperture extraction” results reported in [Fortune et al. \(2025\)](#) compared to our FN-PCA results. For those we get a shallower joint fit eclipse depth than found in the aforementioned paper, although still within  $1\sigma$ .

#### 2.4. TRAPPIST-1 b

Our individual results are consistent with each other within about  $1\sigma$ . The mean of our FN-PCA individual fits agrees with the mean of the individual fits from [Greene et al. \(2023\)](#), and our joint fit result is within error of their joint fit result. Our results differ by over  $1\sigma$  for the individual fits of visits 2 and 3. Our FN-PCA and exponential fits are all within  $1\sigma$  of each other. We



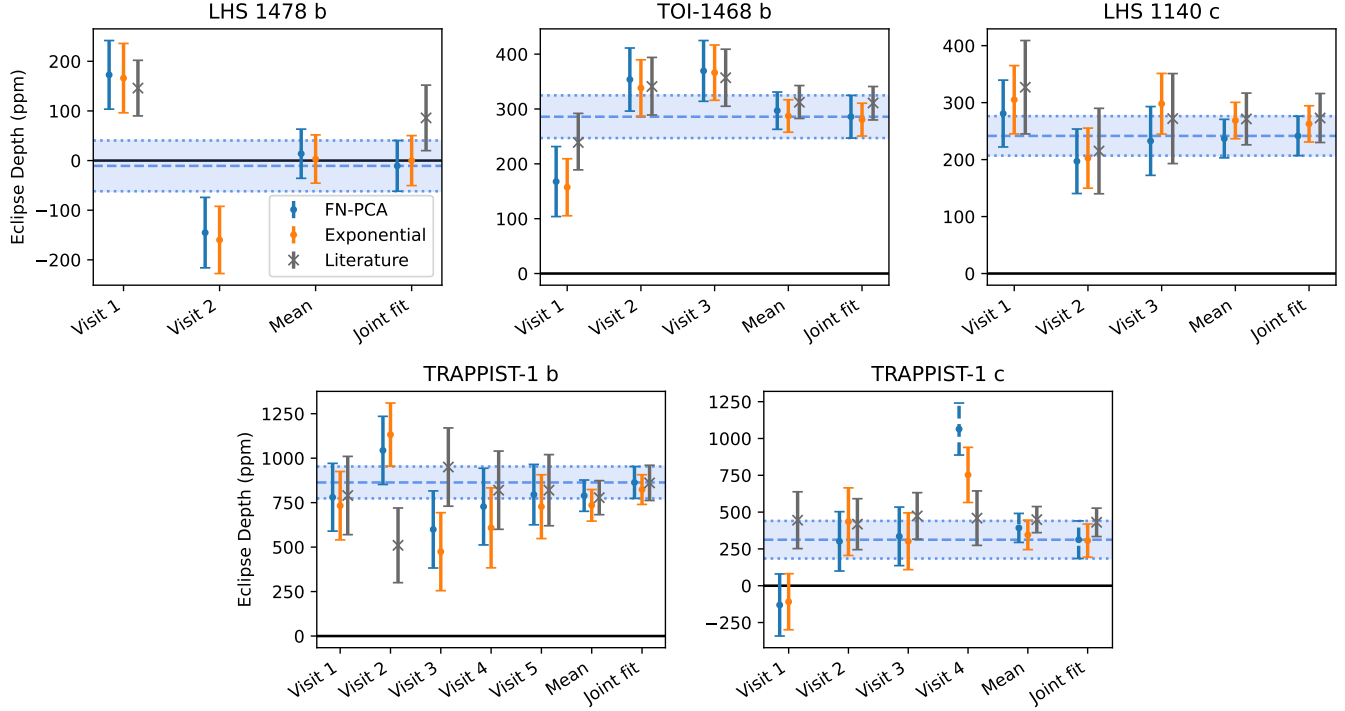


**Figure 2.** Eclipse depths from our reanalysis using the *Erebus* pipeline with FN-PCA and exponential fit detrending, compared to literature values. The joint fit FN-PCA result is shown by the blue dashed line with  $1\sigma$  confidence interval. Exact values used to make this plot are shown in Table 2. The FN-PCA analysis of TRAPPIST-1 c visit 4 (dashed error bar) uses a 2nd degree polynomial to model the stellar variation during the visit.

provide a detailed plot for a single visit of TRAPPIST-1 b (Figure 1) which shows the FN-PCA detrended fit and the components which were detrended against.

### 2.5. TRAPPIST-1 c

The results from *Erebus* produce inconsistent eclipse depths between each visit, including a non-detection for visit 1 (Figure 2). If we adjust the prior to only allow positive eclipse depths, we get a result in agreement with zero for this visit. If we do not force the eclipse depth to be positive for visits 2 and 3, our pipeline mistakes the eclipse egress for a large positive eclipse depth - the eclipse timing for this does not match the timing found in other visits, so we use the positive eclipse depth result. For the FN-PCA analysis of visit 4 we use a 2nd degree polynomial to model stellar variation in the observation that is not detected by the FN-PCA (Figure 2, dashed error bars). Furthermore, our pipeline did not produce results which are in agreement with the values reported in Zieba et al. (2023) for the individual fits of visit 1 and visit 4. This is the case for both the systematic model and the exponential ramp, indicating that the discrepancy is not due to FN-PCA pipeline, but rather some other part of the data reduction process. We further investigated using a four pixel aperture closer in size to that used in Zieba et al. (2023) and find that we still see

a non-detection for visit 1 and a very deep eclipse for visit 4. The joint fit eclipse depth for the 4 pixel aperture reduction is  $337 \pm 141$  ppm, which is in agreement with our five pixel aperture result ( $312 \pm 128$ , Table 2).

## 3. TELESCOPE AND DETECTOR SYSTEMATICS

In order to investigate instrumental behaviour by examining overall trends in the eigenimage and eigenvalue time series produced by FN-PCA, we run the analysis on the published data shown in Section 2, as well as all publicly available  $15 \mu\text{m}$  eclipse data from the Hot Rocks survey (GO 3730 Diamond-Lowe et al. 2024) and a single  $15 \mu\text{m}$  frame normalized observation of LP 791-18 d from GO 6457. Both programs are currently on-going. From this, we group the FN-PCA eigenimages into 4 categories: “detector-settling”, “centroiding”, “pixel-dominated”, and “random”. We investigate the overall trend of the detector-settling component which is present in all of the data.

### 3.1. “Detector-settling” component

All visits have a PC with an eigenimage showing pixel brightness decreasing in the center of the PSF and increasing in the outer portion of the PSF or vice-versa (Figure 3). The eigenvalue is always an exponential ramp.

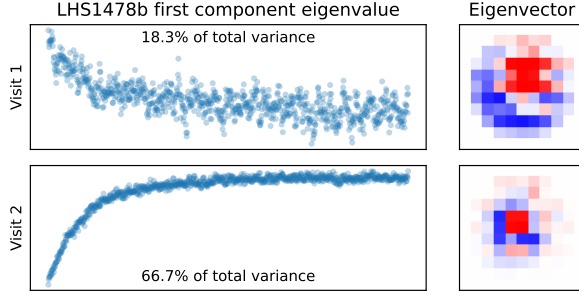


**Figure 3.** The detector settling component either decays with a wide eigenimage covering most of the PSF (top) or ramps up with a more narrow eigenimage (bottom). The ramp-up component is less common and can have a lesser effect on the light curve depending on the size of the aperture and of the affected portion of the PSF due to it being narrower in general, despite being a stronger signal that explains more of the total variance found by PCA.

We found that the detector-settling component can have either a positive or a negative slope (Figure 3) which has similarly been observed in MIRI LRS (Bell et al. 2023, Dyrek et al. 2024). For most visits it is negative (the center of the PSF gets dimmer over the observation). We find that one visit each of TRAPPIST-1 c, LHS 1478 b, and TOI-1468 b, as well as two visits of LHS 1140 c, have a positively sloped detector-settling eigenvalue, where the affected portion of the PSF is much narrower than when the slope is negative (Figure 3, right). For these positive-ramp detector-settling components the eigenvalue ramp is less noisy and the component explains a higher percentage of the total variance within the aperture compared to the negatively-sloped detector-settling components (Figure 3, left). For the visits of TOI-1468 b and LHS 1478 b showing this effect the affected portion of the PSF is entirely encircled by the aperture resulting in a lack of any exponential ramp at the start of the light curve which is seen in other visits (such as the exponential ramp seen for a visit of TRAPPIST-1 b in Figure 1). This effect also does not explain the aberrant visits of TOI-1468 b and LHS 1478 b; the visits showing a shallow/undetected eclipse have the more common negatively-sloped detector-settling component. This is similarly the case for LHS 1140 c, where the eclipse depth is seemingly not correlated to the slope of the detector-settling effect.

In Fortune et al. (2025) they find that the direction of the detector settling slope is related to the filter wavelength of the previous observation. In our analysis we have focused primarily on the length of the settling systematic as we find it to be a more detrimental effect when dealing with systematic noise, as depending on

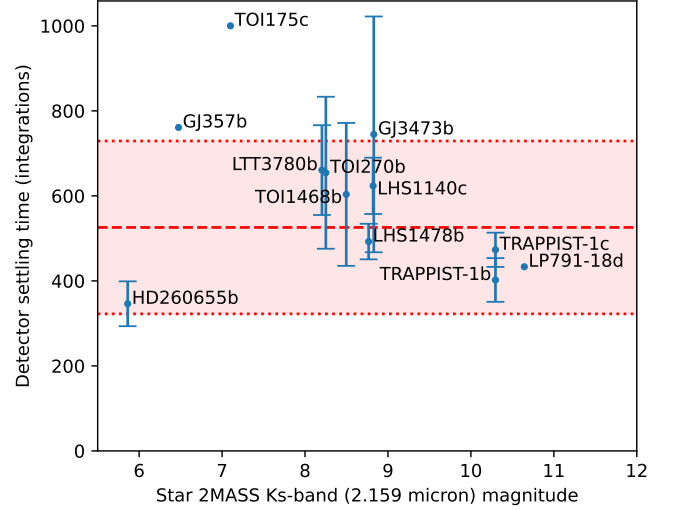


**Figure 4.** The number of integrations for the detector to settle as a function of the star’s Ks band magnitude for all planets with available MIRI 15  $\mu$ m data.  $525 \pm 203$  integrations are required for the detector to settle, which is marked as the red region. TOI175 c appears as a notable outlier, however this data point is based solely on a single available visit and does not take into account possible flux contributions by the two other planets in its star system (Cloutier, R. et al. 2019).

the length of the settling slope the eclipse signal itself can be affected.

We find that the length of the detector-settling eigenvalue is directly related to the magnitude of the star. We modeled the settling ramps with an exponential decay for each visit which was fit using `scipy.optimize.curve_fit` (Figure 5, left). The timescale over-which the exponential ramp stabilizes (99% of the signal decayed) is correlated to the magnitude of the star with an exponential curve (Figure 5, right) given by the equation

$$T_{\text{settling}} = 0.063e^{0.427m_K} - 0.657 \text{ hours.} \quad (3)$$

Due to this strong dependence between photon flux and ramp settling time, we conclude that this first component represents detector settling. For the dimmest stars observed the detector settling time was longer than the observation length. For the brightest stars observed the settling component is replaced by the centroiding components along both diagonal axes as the most prominent sources of systematic noise. We find that  $525 \pm 203$  integrations are required for the detector to fully settle (Figure 4).

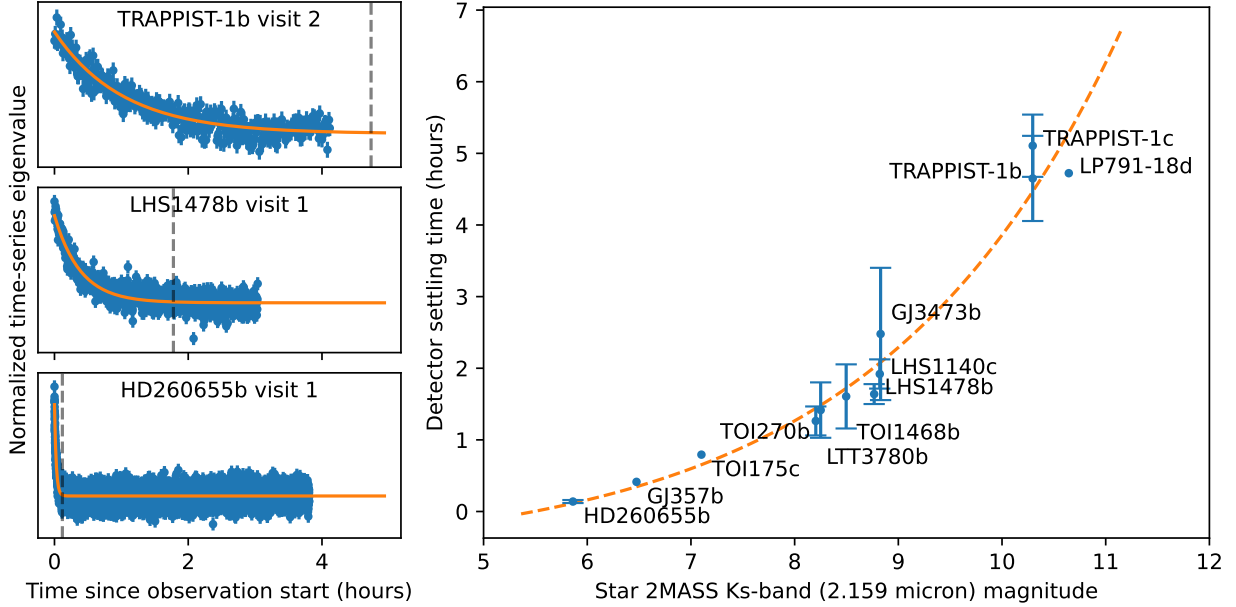


**Figure 5.** (Left) Detector settling time per visit was taken as the time for 99% of the detector-settling component eigenvalue (fit with an exponential) to decay. Three individual visits of planets orbiting high, medium, and low magnitude stars (TRAPPIST-1 b, LHS 1478 b, and HD 260655 b respectively) are shown as examples of detector settling fitting. (Right) Best fit model between detector settling time and star Ks-band magnitude for all planets with available MIRI  $15\ \mu\text{m}$  data. Each data point represents the average settling time across all available visits for that planet, with the error bars taken from the standard deviation of the settling time for all visits (for planets with only a single available visit the error is 0). These data points are generated from: four visits of GJ 3473 b; three visits of LHS 1140 c; two visits of LHS 1478 b; four visits of TOI 270 b; five visits of TRAPPIST-1 b; three visits of TRAPPIST-1 c (we discard one of the four available visits as an outlier); one visit of GJ 357 b; two visits of HD 260655 b; two visits of LTT 3780 b; three visits of TOI 1468 b; one visit of TOI 175 c; and one visit of LP 791-18 d. We label these components as representing detector settling due to their exponential shape and strong dependence on photon flux. For TRAPPIST-1 b (top-left) the settling time is greater than the duration of the observation, for LHS 1478 b (middle-left) the settling time is greater than the midpoint of the observation, and for HD 260655 b (bottom-left) the settling time is near immediate. The best-fit for the detector settling time relationship is:  $T_{\text{settling}} = 0.063e^{0.427m_K} - 0.657$  hours.

### 3.2. “Centroiding” component

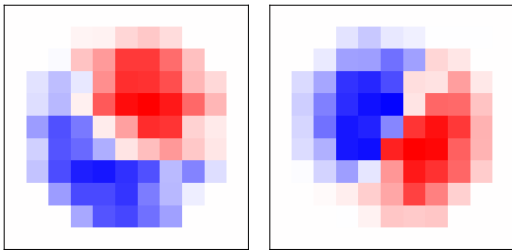


**Figure 6.** The first and fourth principal components of TOI-1468 b visit 1 show the Gaussian centroid moving along two perpendicular axes. The positive diagonal explains 13.9% of the total variance and the negative diagonal explains only 3.6%.

The Gaussian centroid of the PSF moves throughout the visit due to movement of the JWST pointing. This can manifest in two components, each representing movement along a perpendicular axes (Figure 6).

In the majority of visits we investigated, the positive-diagonal axis is the 2nd highest ranked component. For brighter stars the positive-diagonal centroiding component represents the most variance. The 2nd perpendicular centroiding component (negative-diagonal) is always ranked below the positive-diagonal component; in the dimmest star analyzed (TRAPPIST-1) it does not appear in the top 5 highest ranked components, while in the brightest star analyzed (HD260655b) it appears as the 2nd strongest component in all visits. The rank of these components increases as the brightness of the star increases.

### 3.3. “Pixel-dominated” components

The majority of the remaining components for the dimmer stars (K-band magnitude 9 to 12) are pixel-dominated where the eigenimage shows a single pixel being correlated to either another pixel or a group of pixels (Figure 7). These pixel effects may be related to the “Brighter-Fatter Effect” which has been observed in the MIRI detector pixels (Argyriou et al. 2023).



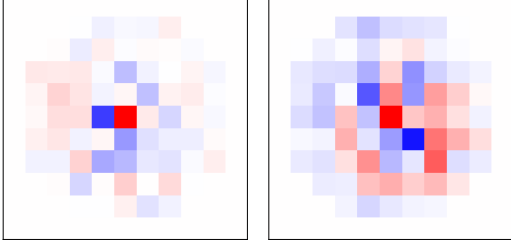


**Figure 7.** Pixel-dominated principal components from visits of TRAPPIST-1 c (left) and TOI-1468 b (right).

### 3.4. “Random” components

This category makes up the rest of the components, which are difficult to categorize by eye. These are more common for the brighter stars (K-band magnitude 5 to 9). Examples are shown in Figure 8.

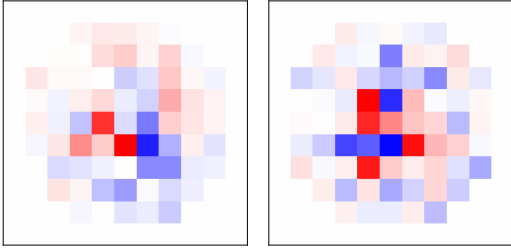


**Figure 8.** Random principal components from two visits of TRAPPIST-1 b.

## 4. ATMOSPHERE AND SURFACE ANALYSIS

We simulated a number of emission spectra for TRAPPIST-1 b, TRAPPIST-1 c, TOI-1468 b, LHS 1478 b, and LHS 1140 c, assuming various bare rock and atmospheric compositions (Figure 9). The bare rock models were chosen to represent a range of potential surface albedos, while the atmosphere models were largely designed to probe the CO<sub>2</sub> absorption band at 15  $\mu$ m. Here we compare them to potential atmospheric and surface models for these planets.

### 4.1. Atmospheric models with SCARLET

The SCARLET modeling framework was employed to generate 1D self consistent atmospheric models (Benneke & Seager 2012, 2013, Benneke 2015, Benneke et al. 2019a,b, Benneke et al. 2024, Pelletier et al. 2021, Pelletier et al. 2024, Roy et al. 2022, 2023, Piaulet-Ghorayeb et al. 2024, Bazinet et al. 2024, Monaghan et al. 2025). These models assume a nongray, radiative, convective temperature profile and a well-mixed composition of 100ppm of CO<sub>2</sub> within an O<sub>2</sub> or H<sub>2</sub>O dominated atmosphere. The models solve for hydrostatic equilibrium and radiative transfer iteratively to produce a the-

oretical temperature-pressure profile of the planet. Once the model converges to stability, the associated emission spectrum from the secondary eclipse is computed. No tidal heating is assumed in these models.

### 4.2. Surface models with JESTER

The bare rock models were calculated using JESTER, which simulates the surface emissions of a bare rock exoplanet given a surface composition and stellar model (Monaghan et al. (in prep.)). The wavelength-dependent hemispherical reflectance of lab samples measured in Paragas et al. (2025) were used to approximate two ultramafic surfaces of varying grain size on each of the five planets, alongside a dark bare rock with zero reflectivity. These values were converted into the corresponding wavelength-dependent emissivity and directional hemispherical reflectance following Hapke theory in order to model the planet’s reflected and emitted surface flux (Hapke 2012). We account for the nonuniform temperature gradient on the planet’s dayside for all bare-rock models by separating the hemisphere into a number of circular regions at an angle  $\theta$  away from the substellar point. The spectral flux density of each region is then calculated such that the sum of the reflected and thermal emission from each region is equal to the incident net flux from the host star onto the annular section (Monaghan et al. 2025). The total spectral flux density of the planet’s dayside is then calculated using the sum of the reflected and emitted flux density, weighted by the area of each annular section.

### 4.3. Treatment of the stellar flux

The models from both SCARLET and JESTER require the use of a stellar model in order to appropriately calculate the planet’s outgoing flux. For consistency, a SPHINX stellar model is used to simulate the host star’s flux for each planet, using an assumed C/O ratio of 0.7. (Iyer et al. 2023, Iyer et al. 2024). The model stellar flux is then used in JESTER to calculate the temperature gradient of the planet and estimate the surface flux density of the planet’s dayside. However, when modeling the expected eclipse depth in Figure 9, the model stellar flux is scaled using the absolute calibrated flux from host star received by Earth in the F1500W filter for each system, measured to be 2.528 mJy for TRAPPIST-1 (Ducrot et al. 2024), 10.54 mJy for TOI-1468 (Valdés et al. 2025), and 9.177 mJy for LHS 1140 Fortune et al. (2025). The expected fluxes of the SPHINX stellar models for each system weighted by the F1500W filter transmission is calculated to be 2.665 mJy for TRAPPIST-1, 11.727 mJy for TOI-1468, and 8.727 mJy for LHS 1140. The stellar flux used in the eclipse depth calculation is

scaled such that the model flux matches the absolute calibrated flux of the host star as measured by MIRI. Note that we do not perform flux recalibration of the models for LHS 1478 b as the SPHINX models were found to suitably model the host star’s flux (August et al. 2024).

#### 4.4. Results

We recalculate the dayside brightness temperature  $T_d$  of each planet using the FN-PCA measured eclipse depths using a simple minimization function. The photon flux  $F_\gamma$  measured in the F1500W filter from the planet (assuming it emits as a uniform temperature blackbody) and host star is calculated as:

$$F_{\gamma,p} = \int \frac{\pi B_p(T_d)\lambda}{hc} W_\lambda d\lambda \quad (4)$$

$$F_{\gamma,star} = \int \frac{F_{star}\lambda}{hc} W_\lambda d\lambda \quad (5)$$

where  $B_p(T_d)$  represents the Planck function,  $W_\lambda$  the throughput of the F1500W filter, and  $F_{star}$  the stellar flux density of the rescaled SPHINX model. For each planet, we find the value  $T_d$  such that  $\frac{R_p^2}{R_{star}^2} \frac{F_{\gamma,p}(T_d)}{F_{\gamma,star}}$  is equal to the FN-PCA measured eclipse depth.

For LHS 1478 b, we compare our surface and atmospheric models to the result of visit 1 due to the inconsistency between visits 1 and 2 and the joint fit detecting no eclipse (Figure 2). From the first visit, we measure a brightness temperature of  $583^{+108}_{-115}$  K, in agreement with the temperature reported by August et al. (2024) of  $491 \pm 102$  K. We rule out a dark bare rock composition at  $\sim 2\sigma$ , and find that the measured eclipse depth is consistent with an atmosphere enriched with CO<sub>2</sub>, similarly to what is concluded in August et al. (2024). For a uniform temperature bare rock with zero heat redistribution ( $f = \frac{2}{3}$ ), the FN-PCA brightness temperature is most consistent with a surface bond albedo  $A_B$  of 0.66, as calculated using:

$$T_d = T_{star} \sqrt{\frac{R_{star}}{a_p}} (1 - A_B)^{\frac{1}{4}} f^{\frac{1}{4}}. \quad (6)$$

Because the second observation had to be discarded, we make no strong conclusions regarding the planet’s composition and await the LHS 1478 b follow up observations in the forthcoming GO 7675 program.

For TOI-1468 b, we find that the planet is hotter than expected for a bare rock (Figure 9) as is found in Valdés et al. (2025). We find a dayside brightness temperature of  $964^{+78}_{-83}$  K, which agrees within  $1\sigma$  of  $1024 \pm 78$  K reported by Valdés et al. (2025). A number of astrophysical and systematic hypotheses are presented by Valdés

et al. (2025) to explain the origin of the measured day-side temperature, including a thermal inversion in the planet’s atmosphere (Miguel et al. 2011, Mackwell et al. 2013, Castan & Menou 2011, Zilinskas et al. 2022), induction heating from the host star’s magnetic field (Vidotto et al. 2014, Shields et al. 2016, Donati et al. 2020, Kislyakova et al. 2018), and unaccounted instrumental artifacts in MIRI (Dyrek et al. 2024, Libralato et al. 2024, Morrison et al. 2023). For the latter, our FN-PCA analysis does not reveal any MIRI systematics that could have deepened the eclipse depth. Future observations are necessary in order to further understand the nature of the deep eclipse.

For LHS 1140 c we measure a dayside brightness temperature of  $528^{+32}_{-36}$  K, which is lower than the value reported by (Fortune et al. 2025) of  $561 \pm 44$  by  $\sim 1\sigma$ . However, our results further rule out an atmospheric presence on the planet, as the FN-PCA eclipse depth is largely consistent with a low-albedo bare rock composition.

For TRAPPIST-1 b we find a dayside brightness temperature of  $499 \pm 24$  K, consistent with both brightness temperatures reported by Greene et al. (2023) and Ducrot et al. (2024) of  $503^{+26}_{-27}$  K and  $478 \pm 27$  K, respectively. Our results further support TRAPPIST-1 b’s composition as an atmosphereless bare rock with a low surface albedo (Ih et al. 2023, Ducrot et al. 2025).

For TRAPPIST-1 c we find a dayside brightness temperature of  $344^{+43}_{-52}$  K. This temperature is lower than the value previously reported in Zieba et al. (2023) of  $380 \pm 31$  K by  $\sim 1\sigma$ , who found that the eclipse depth of the planet was most consistent with a semi-reflective bare rock composition or a thin atmosphere of O<sub>2</sub> and CO<sub>2</sub> (Lincowski et al. 2024). Notably, the FN-PCA eclipse depth further supports the atmospheric scenario for TRAPPIST-1 c, with an eclipse depth consistent with both CO<sub>2</sub> models simulated in Figure 9. Low eclipse depths may also be associated with high albedo clouds within the planet’s atmosphere (Mansfield et al. 2019). Alternatively, highly reflective bare rock surfaces may also be consistent with the measured eclipse depth. Ultramafic surfaces formed by the partial melting of rock are of particular note for planets orbiting M dwarf stars, as the high albedo may lead to false positives for atmospheric detection (Mansfield et al. 2019, Hammond et al. 2025, Paragas et al. 2025).

There are a number of caveats that may affect the accuracy of the simulated emission spectra. Most notably, imperfect knowledge of the stellar spectrum used to simulate the planet’s emission spectra may lead to misleading interpretations of the planet’s composition (e.g., Fauchez et al. 2025, Monaghan et al. (in prep.)).

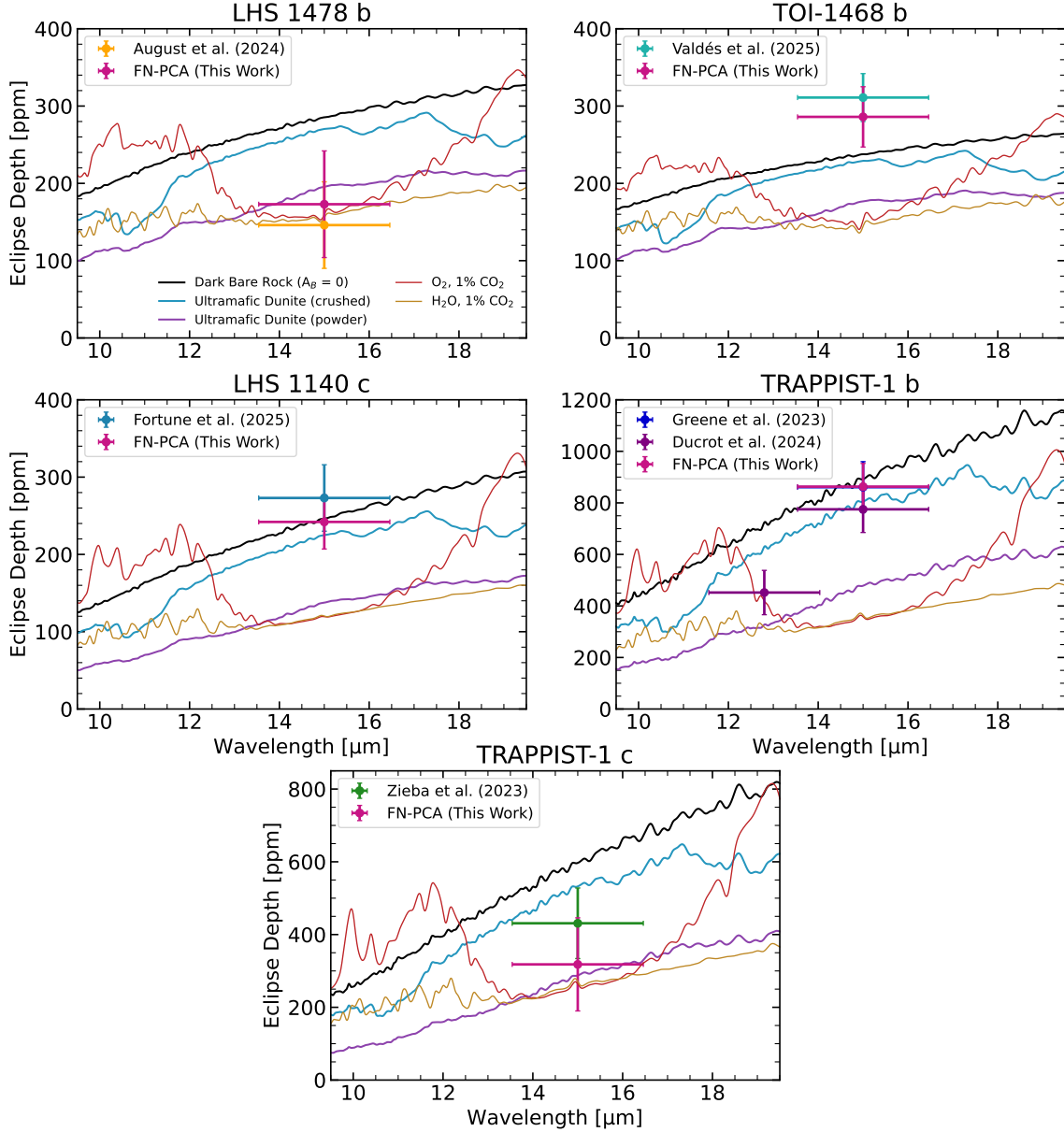


**Figure 9.** Simulated emission spectra for LHS 1478 b, TOI-1468 b, LHS 1140 c, TRAPPIST-1 b, and TRAPPIST-1 c compared to the measured eclipse depths from our FN-PCA calculation, alongside the previous literature results reported in Table 2 (in addition to the values calculated by [Ducrot et al. \(2024\)](#) for TRAPPIST-1 b). The joint fit results are plotted for all planets except for LHS 1478 b, which only plots the measured eclipse depth from the first visit. The Ultramafic Dunite spectra were modeled using the dunite xenolith wavelength-dependent spherical reflectance from [Paragas et al. \(2025\)](#).

Although scaling the stellar model using the absolute flux calibration as outlined in Section 4.3 should result in a more accurate interpretation of the eclipse depth within the MIRI F1500W bandpass, it may lead to inaccuracies outside of the filter’s throughput as we lack knowledge of the host star’s bolometric spectrum. [Fauchez et al. \(2025\)](#) noted that for TRAPPIST-1, although SPHINX models overestimated the star’s mid-IR flux, they were an adequate fit to the star’s flux near-IR

emissions below  $5\mu\text{m}$ , where the majority of the star’s flux is sourced from. It is for this reason that JESTER uses the uncalibrated SPHINX models to simulate the planet’s dayside flux density, as scaling the entirety of the host star’s spectrum beforehand would result in an improperly scaled temperature gradient on the planet’s dayside.

Model accuracy of the simulated atmospheres may be impacted by the presence of clouds, winds, and photo-

chemistry on any of the planets. The mixing ratios of the chosen molecules are also unlikely to be uniform across the planet’s altitude, and other elemental and molecular species unaccounted for in our models may further impact the measured infrared emissions.

For bare rock planets, chemical contaminants, mineralogical mixtures, and space weathering are all known to affect the reflectivity and emissivity of the planet’s surface (e.g., Paragas et al. 2025, Brunetto et al. 2015, Dumusque et al. 2019, Lyu et al. 2024, Mansfield et al. 2019). Furthermore, the emissivity of different mineralogical compositions is largely dependent on temperature (e.g., Helbert et al. 2013, Ferrari et al. 2020, Treiman et al. 2021, Poggiali et al. 2021). Thus, the laboratory spherical reflectance of each composition may not accurately describe the conditions on each planet, which vary in surface temperature. In addition, the surface models provided by Paragas et al. (2025) only provide spherical reflectance for wavelengths shorter than  $20\mu\text{m}$ . Although the contribution of flux from the star above  $20\mu\text{m}$  is small, completely ignoring these wavelengths would result in an artificially inflated dayside temperature (Monaghan et al. (in prep.)). Thus, in order to more accurately account for the energy balance of a true bare rock planet across the entire bolometric wavelength regime, a uniform reflectivity is assumed for the ultramafic surfaces at  $\lambda > 20\mu\text{m}$  of  $\sim 0.35$  and  $\sim 0.5$  for the crushed and powdered surfaces respectively. This modification avoids the overestimation of the planet’s dayside temperature and produces adequate eclipse depth models at  $\lambda < 20\mu\text{m}$ .

## 5. CONCLUSION

We introduced a new lightcurve detrending method, Frame-Normalized Principal Component Analysis (FN-PCA) and showed that it is a viable systematic model for fitting against pixel-level noise in the MIRI  $15\mu\text{m}$  data. We presented a new data reduction pipeline (**Erebus**) which uses this approach to data analysis, which is now ready to be used on the results of the 500 hour Rocky Worlds DDT survey as the data is released. This pipeline is open source at <https://github.com/nicholasconnors/erebus> and easily adaptable to analyze MIRI photometry data in filters other than F1500W.

We reanalyzed results from LHS 1478 b (August et al. 2024), TOI-1468 b (Valdés et al. 2025), LHS 1140 c (Fortune et al. 2025), TRAPPIST-1 b (Greene et al. 2023), and TRAPPIST-1 c (Zieba et al. 2023) using FN-PCA detrending with our **Erebus** pipeline and compared them to different planet surface and atmospheric com-

positions (Figure 9). Using this FN-PCA technique, we provide a deeper insight into the nature of the systematics in the JWST MIRI photometric time series. Furthermore, it provides the advantage that no parameterized form needs to be imposed. We crosscheck our new technique against results previously reported from JWST MIRI data sets, and find that our results are largely in agreement with the aforementioned publications which used conventional parameterized detrending techniques, with the exception of two individual fits each of TRAPPIST-1 c and TRAPPIST-1 b (with the joint fits agreeing within  $1\sigma$ ).

Further looking across multiple data sets, we inspected the eigenvalues for the principal components corresponding to detector settling and calculate a relationship between the detector settling time and target star’s K-band magnitude (Figure 5). For the brightest stars (less than 7 magnitude) the settling time is on the order of minutes, while for the dimmest stars (greater than 11 magnitude) it is on the order of several hours. This relationship can be used to estimate how long a JWST observation must be for the detector-settling to stop being an important source of systematic noise based on the star’s K-band magnitude. This relationship can be used to inform the planning of MIRI F1500W observations for rocky exoplanets in studies like the 500 hour Rocky Worlds DDT.

## ACKNOWLEDGMENTS

We thank the anonymous referee for their thorough review and helpful suggestions which improved this work. All of the data presented in this paper were obtained from the Mikulski Archive for Space Telescopes (MAST) at the Space Telescope Science Institute using the following DOI: [10.17909/h2e9-0j87](https://doi.org/10.17909/h2e9-0j87). N.C. and C.M. acknowledge financial support from the University of Montreal. C.M. further acknowledges financial support from Jean-Marc Lauzon and from the Natural Sciences and Engineering Research Council (NSERC) of Canada. This work was made with the support of the Institut Trottier de Recherche sur les Exoplanètes (iREx).

We used the following code resources in our data analysis: **astropy** (Astropy Collaboration et al. 2013, 2018, 2022), **emcee** (Foreman-Mackey et al. 2013), **NumPy** (Harris et al. 2020), **Eureka!** (Bell et al. 2022), **batman** (Kreidberg 2015), **sklearn** (Pedregosa et al. 2011), **matplotlib** (Hunter 2007), **jwst** (Bushouse et al. 2022), **h5py** (Collette 2013), **SciPy** (Virtanen et al. 2020), **uncertainties**, **pydantic**, and **corner** (Foreman-Mackey 2016).

## REFERENCES

- Agol, E., Dorn, C., Grimm, S. L., et al. 2021, *The Planetary Science Journal*, 2, 1, doi: [10.3847/PSJ/abd022](https://doi.org/10.3847/PSJ/abd022)
- Agol, E., Allen, N. H., Benneke, B., et al. 2024, Updated forecast for TRAPPIST-1 times of transit for all seven exoplanets incorporating JWST data. <https://arxiv.org/abs/2409.11620>
- Ahrer, E.-M., Radica, M., Piaulet-Ghorayeb, C., et al. 2025, *ApJL*, 985, L10, doi: [10.3847/2041-8213/add010](https://doi.org/10.3847/2041-8213/add010)
- Argyriou, I., Lage, C., Rieke, G. H., et al. 2023, *Astronomy & Astrophysics*, 680, A96, doi: [10.1051/0004-6361/202346490](https://doi.org/10.1051/0004-6361/202346490)
- Astropy Collaboration, Robitaille, T. P., Tollerud, E. J., et al. 2013, *A&A*, 558, A33, doi: [10.1051/0004-6361/201322068](https://doi.org/10.1051/0004-6361/201322068)
- Astropy Collaboration, Price-Whelan, A. M., Sipőcz, B. M., et al. 2018, *AJ*, 156, 123, doi: [10.3847/1538-3881/aabc4f](https://doi.org/10.3847/1538-3881/aabc4f)
- Astropy Collaboration, Price-Whelan, A. M., Lim, P. L., et al. 2022, *ApJ*, 935, 167, doi: [10.3847/1538-4357/ac7c74](https://doi.org/10.3847/1538-4357/ac7c74)
- August, P. C., Buchhave, L. A., Diamond-Lowe, H., et al. 2024, Hot Rocks Survey I : A shallow eclipse for LHS 1478 b, arXiv. <http://arxiv.org/abs/2410.11048>
- August, P. C., Buchhave, L. A., Rathcke, A., et al. 2025, Confirming a Tentative Terrestrial Atmosphere Detection on LHS 1478 b with JWST/MIRI, JWST Proposal. Cycle 4, ID. #7675
- Bazinet, L., Pelletier, S., Benneke, B., Salinas, R., & Mace, G. N. 2024, *The Astronomical Journal*, 167, 206, doi: [10.3847/1538-3881/ad3071](https://doi.org/10.3847/1538-3881/ad3071)
- Bell, T. J., Ahrer, E.-M., Brande, J., et al. 2022, *Journal of Open Source Software*, 7, 4503, doi: [10.21105/joss.04503](https://doi.org/10.21105/joss.04503)
- Bell, T. J., Kreidberg, L., Kendrew, S., et al. 2023, A First Look at the JWST MIRI/LRS Phase Curve of WASP-43b. <https://arxiv.org/abs/2301.06350>
- Benneke, B. 2015, Strict Upper Limits on the Carbon-to-Oxygen Ratios of Eight Hot Jupiters from Self-Consistent Atmospheric Retrieval. <https://arxiv.org/abs/1504.07655>
- Benneke, B., Piaulet Ghorayeb, C., & Roy, P.-A. 2024, Thermal emission of a cool, potentially volcanically active exo-Earth, JWST Proposal. Cycle 3, ID. #6457
- Benneke, B., & Seager, S. 2012, *ApJ*, 753, 100, doi: [10.1088/0004-637X/753/2/100](https://doi.org/10.1088/0004-637X/753/2/100)
- . 2013, *ApJ*, 778, 153, doi: [10.1088/0004-637X/778/2/153](https://doi.org/10.1088/0004-637X/778/2/153)
- Benneke, B., Wong, I., Piaulet, C., et al. 2019a, *ApJL*, 887, L14, doi: [10.3847/2041-8213/ab59dc](https://doi.org/10.3847/2041-8213/ab59dc)
- Benneke, B., Knutson, H. A., Lothringer, J., et al. 2019b, *Nature Astronomy*, 3, 813, doi: [10.1038/s41550-019-0800-5](https://doi.org/10.1038/s41550-019-0800-5)
- Benneke, B., Roy, P.-A., Coulombe, L.-P., et al. 2024, JWST Reveals CH<sub>4</sub>, CO<sub>2</sub>, and H<sub>2</sub>O in a Metal-rich Miscible Atmosphere on a Two-Earth-Radius Exoplanet. <https://arxiv.org/abs/2403.03325>
- Bochanski, J. J., Hawley, S. L., Covey, K. R., et al. 2010, *AJ*, 139, 2679, doi: [10.1088/0004-6256/139/6/2679](https://doi.org/10.1088/0004-6256/139/6/2679)
- Brunetto, R., Loeffler, M. J., Nesvorný, D., Sasaki, S., & Strazzulla, G. 2015, in *Asteroids IV*, ed. P. Michel, F. E. DeMeo, & W. F. Bottke (University of Arizona Press), 597–616, doi: [10.2458/azu-uapress.9780816532131-ch031](https://doi.org/10.2458/azu-uapress.9780816532131-ch031)
- Bushouse, H., Eisenhamer, J., Dencheva, N., et al. 2022, JWST Calibration Pipeline, 1.8.2, Zenodo, doi: [10.5281/zenodo.7229890](https://doi.org/10.5281/zenodo.7229890)
- Cadieux, C., Plotnykov, M., Doyon, R., et al. 2023, New Mass and Radius Constraints on the LHS 1140 Planets – LHS 1140 b is Either a Temperate Mini-Neptune or a Water World. <https://arxiv.org/abs/2310.15490>
- Castan, T., & Menou, K. 2011, *The Astrophysical Journal*, 743, L36, doi: [10.1088/2041-8205/743/2/L36](https://doi.org/10.1088/2041-8205/743/2/L36)
- Charbonneau, D., Allen, L. E., Megeath, S. T., et al. 2005, *The Astrophysical Journal*, 626, 523–529, doi: [10.1086/429991](https://doi.org/10.1086/429991)
- Chaturvedi, P., Bluhm, P., Nagel, E., et al. 2022, *A&A*, 666, A155, doi: [10.1051/0004-6361/202244056](https://doi.org/10.1051/0004-6361/202244056)
- Cloutier, R., Astudillo-Defru, N., Bonfils, X., et al. 2019, *A&A*, 629, A111, doi: [10.1051/0004-6361/201935957](https://doi.org/10.1051/0004-6361/201935957)
- Collette, A. 2013, *Python and HDF5* (O'Reilly)
- Coulombe, L.-P., Benneke, B., Challener, R., et al. 2023, *Nature*, 620, 292, doi: [10.1038/s41586-023-06230-1](https://doi.org/10.1038/s41586-023-06230-1)
- Coulombe, L.-P., Radica, M., Benneke, B., et al. 2025, *Nature Astronomy*, doi: [10.1038/s41550-025-02488-9](https://doi.org/10.1038/s41550-025-02488-9)
- Coy, B. P., Ih, J., Kite, E. S., et al. 2025, Population-level Hypothesis Testing with Rocky Planet Emission Data: A Tentative Trend in the Brightness Temperatures of M-Earths. <https://arxiv.org/abs/2412.06573>
- de Wit, J., Doyon, R., Rackham, B. V., et al. 2024, *Nature Astronomy*, 8, 810–818, doi: [10.1038/s41550-024-02298-5](https://doi.org/10.1038/s41550-024-02298-5)
- Diamond-Lowe, H., Mendonca, J. M., Buchhave, L. A., et al. 2024. <https://www.stsci.edu/jwst/phase2-public/3730.pdf>
- Donati, J. F., Kouach, D., Moutou, C., et al. 2020, *MNRAS*, 498, 5684, doi: [10.1093/mnras/staa2569](https://doi.org/10.1093/mnras/staa2569)
- Ducrot, E., Gillon, M., Delrez, L., et al. 2020, *A&A*, 640, A112, doi: [10.1051/0004-6361/201937392](https://doi.org/10.1051/0004-6361/201937392)
- Ducrot, E., Lagage, P.-O., Min, M., et al. 2024, *Nature Astronomy*, 9, 358–369, doi: [10.1038/s41550-024-02428-z](https://doi.org/10.1038/s41550-024-02428-z)
- . 2025, *Nature Astronomy*, 9, 358–369, doi: [10.1038/s41550-024-02428-z](https://doi.org/10.1038/s41550-024-02428-z)



- Dumusque, X., Turner, O., Dorn, C., et al. 2019, *A&A*, 627, A43, doi: [10.1051/0004-6361/201935457](https://doi.org/10.1051/0004-6361/201935457)
- Dyrek, A., Ducrot, E., Lagage, P.-O., et al. 2024, *Astronomy & Astrophysics*, 683, A212, doi: [10.1051/0004-6361/202347127](https://doi.org/10.1051/0004-6361/202347127)
- Faucher, T. J., Rackham, B. V., Ducrot, E., Stevenson, K. B., & de Wit, J. 2025, *Stellar Models Also Limit Exoplanet Atmosphere Studies in Emission*. <https://arxiv.org/abs/2502.19585>
- Ferrari, S., Maturilli, A., Carli, C., et al. 2020, *Earth and Planetary Science Letters*, 534, 116089, doi: [10.1016/j.epsl.2020.116089](https://doi.org/10.1016/j.epsl.2020.116089)
- Foreman-Mackey, D. 2016, *Journal of Open Source Software*, 1, 24, doi: [10.21105/joss.00024](https://doi.org/10.21105/joss.00024)
- Foreman-Mackey, D., Hogg, D. W., Lang, D., & Goodman, J. 2013, *Publications of the Astronomical Society of the Pacific*, 125, 306–312, doi: [10.1086/670067](https://doi.org/10.1086/670067)
- Fortune, M., Gibson, N. P., Diamond-Lowe, H., et al. 2025, *Hot Rocks Survey III: A deep eclipse for LHS 1140c and a new Gaussian process method to account for correlated noise in individual pixels*. <https://arxiv.org/abs/2505.22186>
- Gelman, A., & Rubin, D. B. 1992, *Statistical Science*, 7, 457, doi: [10.1214/ss/1177011136](https://doi.org/10.1214/ss/1177011136)
- Greene, T. P., Bell, T. J., Ducrot, E., et al. 2023, *Nature*, 618, 39, doi: [10.1038/s41586-023-05951-7](https://doi.org/10.1038/s41586-023-05951-7)
- Grimm, S. L., Demory, B.-O., Gillon, M., et al. 2018, *A&A*, 613, A68, doi: [10.1051/0004-6361/201732233](https://doi.org/10.1051/0004-6361/201732233)
- Hammond, M., Guimond, C. M., Lichtenberg, T., et al. 2025, *The Astrophysical Journal Letters*, 978, L40, doi: [10.3847/2041-8213/ada0bc](https://doi.org/10.3847/2041-8213/ada0bc)
- Hapke, B. 2012, *Theory of Reflectance and Emittance Spectroscopy*, 2nd edn. (Cambridge University Press)
- Harris, C. R., Millman, K. J., van der Walt, S. J., et al. 2020, *Nature*, 585, 357, doi: [10.1038/s41586-020-2649-2](https://doi.org/10.1038/s41586-020-2649-2)
- Helbert, J., Nestola, F., Ferrari, S., et al. 2013, *Earth and Planetary Science Letters*, 371, 252, doi: [10.1016/j.epsl.2013.03.038](https://doi.org/10.1016/j.epsl.2013.03.038)
- Hunter, J. D. 2007, *Computing in Science & Engineering*, 9, 90, doi: [10.1109/MCSE.2007.55](https://doi.org/10.1109/MCSE.2007.55)
- Ih, J., Kempton, E. M.-R., Whittaker, E. A., & Lessard, M. 2023, *ApJL*, 952, L4, doi: [10.3847/2041-8213/ace03b](https://doi.org/10.3847/2041-8213/ace03b)
- Iyer, A., Line, M., Muirhead, P., Fortney, J., & Gharib-Nezhad, E. 2024, in *AAS/Division for Extreme Solar Systems Abstracts*, Vol. 56, AAS/Division for Extreme Solar Systems Abstracts, 631.03
- Iyer, A. R., Line, M. R., Muirhead, P. S., Fortney, J. J., & Gharib-Nezhad, E. 2023, *The Astrophysical Journal*, 944, 41, doi: [10.3847/1538-4357/acabc2](https://doi.org/10.3847/1538-4357/acabc2)
- Kislyakova, K. G., Fossati, L., Johnstone, C. P., et al. 2018, *The Astrophysical Journal*, 858, 105, doi: [10.3847/1538-4357/aabae4](https://doi.org/10.3847/1538-4357/aabae4)
- Kokori, A., Tsiaras, A., Edwards, B., et al. 2023, *The Astrophysical Journal Supplement Series*, 265, 4, doi: [10.3847/1538-4365/ac9da4](https://doi.org/10.3847/1538-4365/ac9da4)
- Koll, D. D. B. 2022, *The Astrophysical Journal*, 924, 134, doi: [10.3847/1538-4357/ac3b48](https://doi.org/10.3847/1538-4357/ac3b48)
- Kreidberg, L. 2015, *PASP*, 127, 1161, doi: [10.1086/683602](https://doi.org/10.1086/683602)
- Libralato, M., Argyriou, I., Dicken, D., et al. 2024, *High-precision astrometry and photometry with the JWST/MIRI imager*. <https://arxiv.org/abs/2311.12145>
- Lincowski, A., Virtual Planetary Laboratory, Meadows, V., et al. 2024, in *AAS/Division for Extreme Solar Systems Abstracts*, Vol. 56, AAS/Division for Extreme Solar Systems Abstracts, 627.10
- Luger, R., & Barnes, R. 2015, *Astrobiology*, 15, 119, doi: [10.1089/ast.2014.1231](https://doi.org/10.1089/ast.2014.1231)
- Lyu, X., Koll, D. D. B., Cowan, N. B., et al. 2024, *The Astrophysical Journal*, 964, 152, doi: [10.3847/1538-4357/ad2077](https://doi.org/10.3847/1538-4357/ad2077)
- Mackwell, S. J., Simon-Miller, A. A., Harder, J. W., & Bullock, M. A. 2013, *Comparative Climatology of Terrestrial Planets* (University of Arizona Press), doi: [10.2458/azu\\_uapress.9780816530595](https://doi.org/10.2458/azu_uapress.9780816530595)
- Mansfield, M., Kite, E. S., Hu, R., et al. 2019, *The Astrophysical Journal*, 886, 141, doi: [10.3847/1538-4357/ab4c90](https://doi.org/10.3847/1538-4357/ab4c90)
- Miguel, Y., Kaltenegger, L., Fegley, B., & Schaefer, L. 2011, *ApJL*, 742, L19, doi: [10.1088/2041-8205/742/2/L19](https://doi.org/10.1088/2041-8205/742/2/L19)
- Monaghan, C., Roy, P.-A., Benneke, B., et al. 2025, *The Astronomical Journal*, 169, 239, doi: [10.3847/1538-3881/adbe75](https://doi.org/10.3847/1538-3881/adbe75)
- Morrison, J. E., Dicken, D., Argyriou, I., et al. 2023, *Publications of the Astronomical Society of the Pacific*, 135, 075004, doi: [10.1088/1538-3873/acdea6](https://doi.org/10.1088/1538-3873/acdea6)
- Nutzman, P., & Charbonneau, D. 2008, *PASP*, 120, 317, doi: [10.1086/533420](https://doi.org/10.1086/533420)
- Paragas, K., Knutson, H. A., Hu, R., et al. 2025, *The Astrophysical Journal*, 981, 130, doi: [10.3847/1538-4357/ada9eb](https://doi.org/10.3847/1538-4357/ada9eb)
- Pedregosa, F., Varoquaux, G., Gramfort, A., et al. 2011, *Journal of Machine Learning Research*, 12, 2825
- Pelletier, S., Benneke, B., Darveau-Bernier, A., et al. 2021, *AJ*, 162, 73, doi: [10.3847/1538-3881/ac0428](https://doi.org/10.3847/1538-3881/ac0428)
- Pelletier, S., Benneke, B., Chachan, Y., et al. 2024, *The Astronomical Journal*, 169, 10, doi: [10.3847/1538-3881/ad8b28](https://doi.org/10.3847/1538-3881/ad8b28)

- Piaulet-Ghorayeb, C., Benneke, B., Radica, M., et al. 2024, *The Astrophysical Journal Letters*, 974, L10, doi: [10.3847/2041-8213/ad6ff0](https://doi.org/10.3847/2041-8213/ad6ff0)
- Poggiali, G., Brucato, J. R., Dotto, E., et al. 2021, *Icarus*, 354, 114040, doi: [10.1016/j.icarus.2020.114040](https://doi.org/10.1016/j.icarus.2020.114040)
- Rackham, B. V., Apai, D., & Giampapa, M. S. 2018, *ApJ*, 853, 122, doi: [10.3847/1538-4357/aaa08c](https://doi.org/10.3847/1538-4357/aaa08c)
- Radica, M., Coulombe, L.-P., Taylor, J., et al. 2024, *ApJL*, 962, L20, doi: [10.3847/2041-8213/ad20e4](https://doi.org/10.3847/2041-8213/ad20e4)
- Radica, M., Piaulet-Ghorayeb, C., Taylor, J., et al. 2025, *ApJL*, 979, L5, doi: [10.3847/2041-8213/ada381](https://doi.org/10.3847/2041-8213/ada381)
- Redfield, S., Batalha, N., Benneke, B., et al. 2024, *arXiv e-prints*, arXiv:2404.02932, doi: [10.48550/arXiv.2404.02932](https://doi.org/10.48550/arXiv.2404.02932)
- Roy, P.-A., Benneke, B., Piaulet, C., et al. 2022, *The Astrophysical Journal*, 941, 89, doi: [10.3847/1538-4357/ac9f18](https://doi.org/10.3847/1538-4357/ac9f18)
- . 2023, *The Astrophysical Journal Letters*, 954, L52, doi: [10.3847/2041-8213/acebf0](https://doi.org/10.3847/2041-8213/acebf0)
- Shields, A. L., Ballard, S., & Johnson, J. A. 2016, *PhR*, 663, 1, doi: [10.1016/j.physrep.2016.10.003](https://doi.org/10.1016/j.physrep.2016.10.003)
- Shlens, J. 2014, A Tutorial on Principal Component Analysis. <https://arxiv.org/abs/1404.1100>
- Soto, M. G., Anglada-Escudé, G., Dreizler, S., et al. 2021, *A&A*, 649, A144, doi: [10.1051/0004-6361/202140618](https://doi.org/10.1051/0004-6361/202140618)
- Treiman, A. H., Filiberto, J., & Vander Kaaden, K. E. 2021, *Planetary Science Journal*, 2, 43, doi: [10.3847/PSJ/abd546](https://doi.org/10.3847/PSJ/abd546)
- Turbet, Martin, Bolmont, Emeline, Leconte, Jeremy, et al. 2018, *A&A*, 612, A86, doi: [10.1051/0004-6361/201731620](https://doi.org/10.1051/0004-6361/201731620)
- Valdés, E. A. M., Demory, B. O., Diamond-Lowe, H., et al. 2025, *Hot Rocks Survey II: The thermal emission of TOI-1468 b reveals a hot bare rock*. <https://arxiv.org/abs/2503.19772>
- Vidotto, A. A., Gregory, S. G., Jardine, M., et al. 2014, *MNRAS*, 441, 2361, doi: [10.1093/mnras/stu728](https://doi.org/10.1093/mnras/stu728)
- Virtanen, P., Gommers, R., Oliphant, T. E., et al. 2020, *Nature Methods*, 17, 261, doi: [10.1038/s41592-019-0686-2](https://doi.org/10.1038/s41592-019-0686-2)
- Zieba, S., Kreidberg, L., Ducrot, E., et al. 2023, *Nature*, 620, 746, doi: [10.1038/s41586-023-06232-z](https://doi.org/10.1038/s41586-023-06232-z)
- Zilinskas, M., van Buchem, C. P. A., Miguel, Y., et al. 2022, *Astronomy & Astrophysics*, 661, A126, doi: [10.1051/0004-6361/202142984](https://doi.org/10.1051/0004-6361/202142984)